NUMERICAL SIMULATION OF HIGH LIFT CONFIGURATIONS USING UNSTRUCTURED MESH METHOD

Mitsuhiro MURAYAMA* and Kazuomi YAMAMOTO*
***Institute of Space Technology and Aeronautics, Japan Aerospace Exploration Agency**

Keywords: *high-lift configurations, CFD, unstructured mesh*

Abstract

In this paper, computations of 2D/3D high-lift configurations are performed on structured and unstructured meshes for improvement of the accuracy of the flow analyses. Computations of a 2D two-element NLR-7301 airfoil are performed to investigate influence of outer boundary location and mesh dependency. Mesh dependency on unstructured meshes is examined using a mesh refinement approach by changing regions for mesh refinement. The results show the mesh density away from the wing surface is required for drag prediction by the flows around high-lift devises that have large circulation and wake. Next, computations of a 3D three-element wing-fuselage configuration are performed. Computed C_L and C_D on structured and unstructured meshes show good agreement with the experimental data. However, it is also shown that further mesh refinement on unstructured meshes should be used to improve the resolution for slat wake, wing tip, and trailing edge for more accurate prediction.

1 Introduction

In Japan, momentum toward development of small commercial jet airplanes has been increasing recently. In the airplane design, the development of efficient high-lift devices is one of the important requirements for successful design. Improvements of the high-lift devices have strong impacts on the performance of an aircraft. On a general commercial jet aircraft, 1% improvement of the lift-to-drag ratio at take-off allows 2800lb increase in payload and 1.5% improvement of the maximum lift coefficients at landing allows 6600lb increase in payload [1].

For many years, high-lift devices have been empirically designed using theoretical analyses and wind tunnel tests. By recent developments of CFD and optimization algorithm, the aerodynamic optimization using CFD is highly expected to improve the performance [2-4]. In general, multi-element wing system, such as slat, main, and flap elements, is utilized as high-lift devices. However, the high-lift configurations considerably complicate the flow physics by boundary layer transition, separations and re-attachments. In addition, CFD mesh generation around the high-lift configurations is troublesome due to the complexity of the configurations. For the aerodynamic optimization, problems associated with the mesh generation and the accuracy has to be addressed.

Unstructured mesh method has capability to handle the complicated configurations associated with high-lift devices. For the practical aerodynamic design optimization on a complex three-dimensional geometry, the computational mesh has to be efficiently modified according to the geometry modification by the optimization. An efficient and robust dynamic mesh method to modify unstructured meshes has been developed by one of the present authors [5,6]. In addition, unstructured mesh system has the flexibility to use adaptive mesh refinement method to address the problems associated with the mesh resolution [7].

Currently, CFD has achieved a great progress in the computation of flows around airplanes at cruise conditions. On the contrary, it is still difficult to deal with complex flows at off-design conditions where flow separates and

vortices characterize the flow features, especially when the high-lift system is deployed. However, for development of an efficient aerodynamic optimization system, the accuracy of unstructured mesh CFD for high-lift system has to be clarified and the improvement of the reliability is required. In this paper, for the purpose, computations of 2D/3D high-lift configurations are performed and the reliability is clarified. Computations both on structured mesh and unstructured mesh are performed and the computational results are validated. By comparison with the results, some ways to improve the reliability on structured and unstructured meshes are discussed.

2 Flow Solvers

As an unstructured mesh generator and a flow solver, TAS (Tohoku University Aerodynamic Simulation) code [8] is used in this study.

TAS_Mesh is the mesh generator of triangular surface mesh with the advancing front method using graphical user interface (GUI) tools [9,10], tetrahedral volume mesh using Delaunay tetrahedral meshing [11], and hybrid volume mesh composed of tetrahedrons, prisms, and pyramids for high Reynolds number viscous flows [12].

In TAS_Flow, Navier-Stokes equations are solved on the unstructured mesh by a cell-vertex finite volume method. HLLEW method [13] is used for the numerical flux computations. Second-order spatial accuracy is realized by a liner reconstruction of the primitive variables. LU-SGS implicit method [14] is used for the time integration. Spalart-Allmaras turbulence model [15] is used in the present computations.

As the flow solver on multi-block structured meshes, UPACS is used. UPACS is a standard CFD code in JAXA Institute of Space Technology and Aeronautics (ISTA) [16]. The solver of UPACS is based on a cell-centered finite volume method. Roe's flux difference scheme for convection terms, MFGS (Matrix Free Gauss Seidel) implicit method for the time integration, and Spalart-Allmaras turbulence model are used in the present computations.

For 2D problems, computational meshes consist of a layer of prisms generated by stacking a triangular mesh in the case of unstructured meshes and hexahedrons generated by stacking a rectangular mesh in the case of structured meshes to use 3D codes.

All computations are accomplished using multi-processors of Fujitsu PRIMEPOWER HPC2500, which is the central machine of Numerical Simulator III system in ISTA/JAXA [17].

3 Results

3.1 Two-Dimensional Two-Element NLR-7301 Airfoil

3.1.1 Computational Model

First, computations of a 2-D two-element airfoil are performed. The geometry used in this study is NLR-7301 airfoil [18] shown in Fig. 1. The flap angle, δ_F, is set to moderate value 20° and the gap width between main section and flap is 1.3% of c where c is the chord of the basic NLR-7301 airfoil. The overlap of the main wing section and the flap, O/L, is 5.3% of c. Freestream Mach number is 0.185 and the Reynolds number is 2.51×10^6. All turbulent flow is assumed in the computations.

3.1.2 Computational Results

3.1.2.1 Influence of Outer Boundary Location

Three unstructured meshes, *UG-Near*, *UG-Medium*, and *UG-Far*, whose outer boundaries are located 13-, 50-, and 100-chord length away from the body surface are prepared to investigate influence of locations of outer boundary on the computational results. The location of outer boundaries on *UG-Near* is same as a structured mesh provided for a workshop to validate CFD codes and assessment of turbulence models in Ref. 18.

The meshes have 1074 mesh points on the main wing and 1476 points on the flap wing. On the blunt trailing-edge, about 25 mesh points are located. The minimum spacing in the normal direction to the wing surface is 1×10^{-5}. All the

meshes have about 0.16 million mesh points. Figure 1 shows the computational mesh of *UG-Near*.

Figure 2 shows the total drag coefficients, C_D, and the components separated into pressure drag, C_{Dp}, friction drag, C_{Df}, total drag on the main wing, C_{Dmain}, and total drag on the flap wing, C_{Dflap}, at angle of attack (α) of 6°.

By comparison between the results at *-Near* and *-Far* meshes, it is shown that C_{Dmain} and C_{Dp} at *-Far* meshes are largely decreased by about 100 drag counts (1 drag count = 1×10^{-4}). On the other hand, difference of C_D between the results at *-Medium* and *-Far* is only a few drag counts. It was apparently shown that outer boundaries should be located at least 50-chord length away from the body surface to predict drag. The outer boundary location of *UG-Near* is not so close. However, the influence on the drag prediction is so large. Flows around high-lift devises have large circulation and wake. In such flows, large computational domains are required to decrease the influence of outer boundaries.

Figure 3 shows variations of lift coefficients (C_L) versus angle of attack (C_L-α). Surface pressure coefficients (C_P) at α=6° are shown in Fig. 4. By extent of far field boundaries, trends of C_L are shift to high values and angles of attack to stall are changed. While, from the distributions of C_P, variance of suction peak and lift increment on the main wing can be seen and the results show better agreement with experimental results.

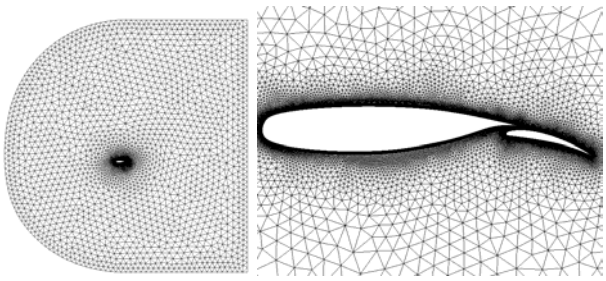

(a) Full view (b) Close-up view

Fig. 1 Unstructured mesh (*UG-Near*)

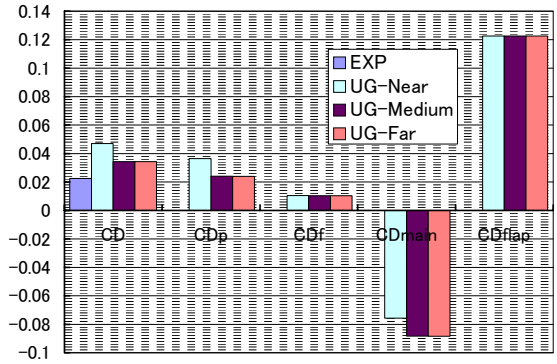

Fig. 2 Comparison of drag components by the difference of outer boundary location at angle of attack (α) of 6°

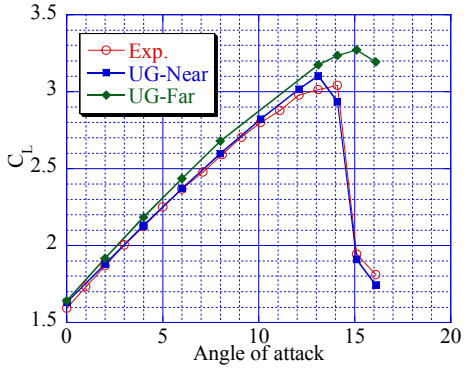

Fig. 3 Variations of lift coefficients (C_L) versus angle of attack (α) by outer boundary location

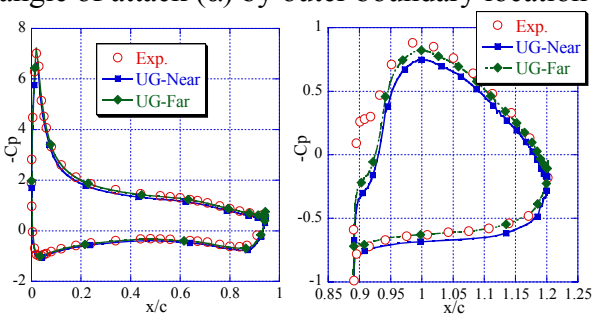

Fig. 4 Variations of surface pressure coefficients (C_P) by outer boundary location at α=6°

3.1.2.2 Influence of Mesh Density

To examine the mesh dependency on structured meshes, three multi-block structured meshes, *SG-Fine*, *SG-Medium*, and *SG-Coarse* are generated. *SG-Fine* is a mesh whose outer boundaries are located 100 chord length away from the body surface. The minimum spacing in normal direction to the wing surface is 6×10^{-6}. The mesh has about 0.8 million mesh points. *SG-Medium* and *SG-Coarse* have 1/4 and 1/16 mesh points of *SG-Fine*, which are generated by pulling out mesh points from *SG-Fine* in both *i*

and j direction. Figure 5 shows the meshes near the leading edge of the main wing.

Figure 6 and 7 show variations of C_L-α and C_L- C_D by the difference of mesh density. In the results on *SG-Coarse*, the discrepancy of C_L appears near stall angle of attack and C_D are over-predicted overall. Discrepancy between *SG-Fine* and *SG-Medium* is not large. Figure 8 shows the mesh convergence on C_D. The differences between *SG-Fine* and *SG-Medium* are only 3-10 drag counts (1 drag count = 1×10^{-4}) and the mesh convergence can be seen. Results using the following Richardson Extrapolation [19],

$$f[exact] \fallingdotseq 4/3 f_1 - 1/3 f_2 \quad (1)$$

where f_1 and f_2 are solutions of fine mesh (h_1) and coarse mesh (h_2), are also shown in Fig. 8. It can be seen that the extrapolation predicts C_D convergence. The results on *SG-Fine* are very close to the converged results. Therefore, the results on *SG-Fine* are utilized to compare and discuss the results on unstructured meshes.

To examine the mesh dependency on unstructured meshes, a mesh refinement method based on a bisection algorithm [20] is utilized to increase mesh points. *UG-Far* mesh is utilized as the baseline mesh, *UG*. Regions that require more mesh points are investigated by changing regions for mesh refinement. The information of refined meshes is summarized in Table 1. Figures 9-12 show the meshes.

C_D, C_{Dp}, and, C_{Df} obtained at each mesh are shown in Fig. 13. Compared with the result at *UG-2* where mesh points are increased in the regions near the flap wing, the result at *UG-3* shown in Fig. 9 where mesh points are increased in all regions 2-chord length away from the wing shows great improvement of drag prediction. C_D at *UG* is larger than at *SG-Fine* by about 80 drag counts, while about 60 drag counts reduction of pressure drag can be seen at *UG-3*.

Next, to examine the mesh density within 2-chord length, the following two meshes are prepared. *UG-4* shown in Fig. 10 is a mesh where mesh points are additionally increased in the regions around the half of the main wing on *UG-3*. *UG-5* shown in Fig. 11 is a mesh where the same regions as *UG-3* are refined again. Difference of C_D between the results at *UG-3*, *UG-4*, and *UG-5* is only a few drag counts as shown in Fig. 13. The mesh density within 2-chord length away from the wing is proven to be enough on *UG-3*.

UG-3, *UG-6*, *UG-7*, and *UG-8* are computational meshes where the refined regions are extended to regions 2-, 4-, 20-, and 50-chord length away from the wing. On each mesh, about 60, 70, 80, and 80 drag counts reduction of pressure drag from the result on *UG* can be seen. Difference of C_D between *UG-7* and *UG-8* is within one drag count. These results show the importance of the mesh density away from the wing. On *UG-9* and *UG-10*, the number of the mesh points on the main wing and flap wing is doubled. As shown in Fig. 13, however, the differences of C_D between *UG* and *UG-9* are not so large and results on *UG-8* and *UG-10* are almost same. It also shows the importance of the mesh density away from the wing surface. On unstructured meshes, the mesh tends to become coarser rapidly in the regions away from the wing surface. Flows around high-lift devises have large circulation and wake. Therefore, the flows still change in the regions away from the wing surface. However, if the mesh size is too large, the flow changes cannot be captured. Then, the loss of total pressure and non-physical production of entropy will occur in the regions. On structured meshes, the mesh density away from the wing surface is still higher by limitation of the topology of structured meshes.

Figure 14 shows the contours of variation of entropy. The variation of entropy, $\Delta s/R$, is defined as follows;

$$\frac{\Delta s}{R} = \frac{1}{\gamma - 1} \ln\left[\frac{p}{p_\infty}\left(\frac{\rho_\infty}{\rho}\right)^\gamma\right] \quad (2)$$

where p, ρ, and γ are pressure, density, and specific heat ratio and subscript, ∞, represents the value of the physical variables in freestream. In Fig. 14, the range of the contours is extremely narrowed and the variations are much highlighted. In general, entropy increments can be seen in the boundary layers and after the generation of shock waves. In Figs. 14(a) and 14(b), the entropy is non-physically increased in

the regions far away from the wing surface by the numerical errors. On *UG* mesh, non-physical increments of the entropy are so large and we can see that the mesh resolution is not enough, easily. By the extension of refined regions, the entropy increments become smaller as shown in Figs. 14(d) and 14(f).

Figures 15 and 16 show comparison of C_L-α and C_L-C_D between on *SG-Fine*, *UG*, and *UG-8*. By proper distributions of mesh points, the flow analyses on unstructured meshes are comparable to the results on structured meshes. In this study, relatively rough and wide regions are selected for refined regions to clarify the mesh dependency. The monitor using this entropy increment can be a candidate for mesh refinement indicator. By clarifying physically important regions and regions where such numerical errors should be decreased, mesh points on unstructured meshes can be decreased.

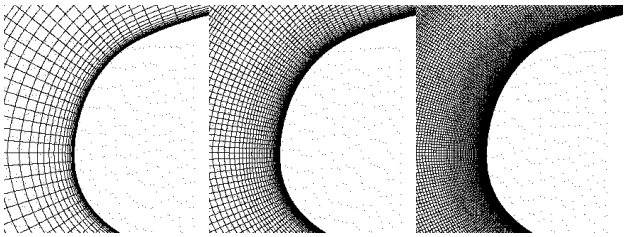

(a) *SG-Coarse* (b) *SG-Medium* (c) *SG-Fine*

Fig. 5 Close-up view of structured meshes near the leading edge of the main wing

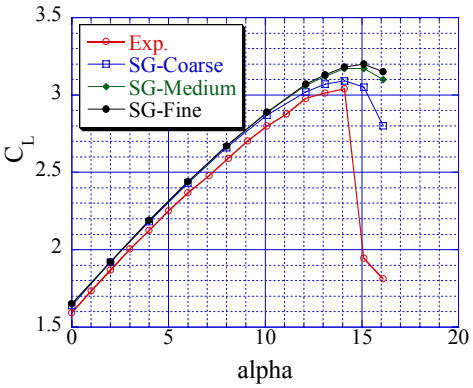

Fig. 6 Variation of C_L-α by mesh density on structured mesh

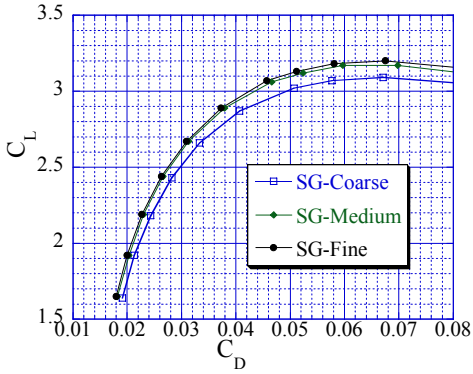

Fig. 7 Variation of C_L-C_D by mesh density on structured mesh

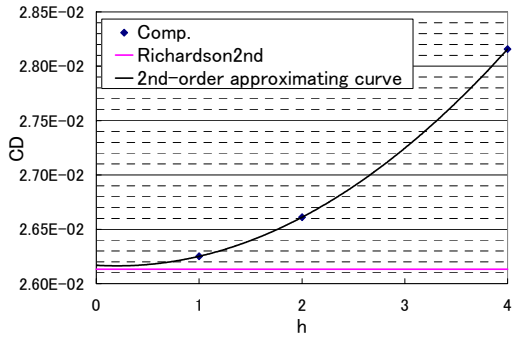

(a) α=6°

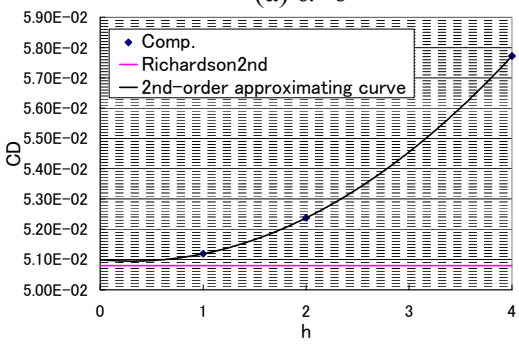

(b) α=13.1°

Fig. 8 Mesh convergence of drag on structured meshes

Table 1 Refined regions on unstructured mesh

	Mesh points ($\times 10^6$)	Refined regions
UG	0.16	Baseline mesh for mesh refinement
UG-2	0.26	Near the flap wing
UG-3	0.4	2-chord length away from the wing
UG-4	0.7	Around the half of the main wing on UG-3
UG-5	1	2-chord length away from the wing on UG-3
UG-6	0.46	4-chord length away from the wing
UG-7	0.49	20-chord length away from the wing
UG-8	0.5	50-chord length away from the wing
UG-9	0.28	Mesh points on the wings are double as many as UG
UG-10	0.66	50-chord length away from the wing on UG-9

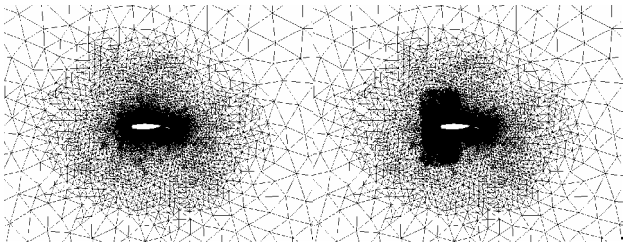

Fig. 9 *UG-3* mesh

Fig.10 *UG-4* mesh

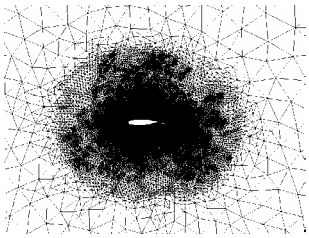

Fig. 11 *UG-5* mesh

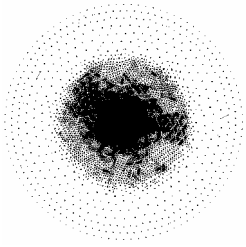

Fig.12 *UG-8* mesh

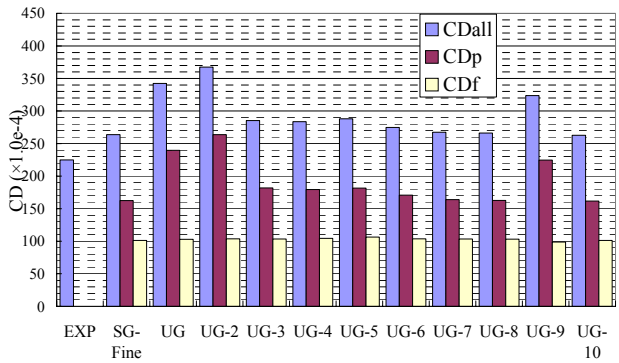

Fig. 13 Comparison of drag components

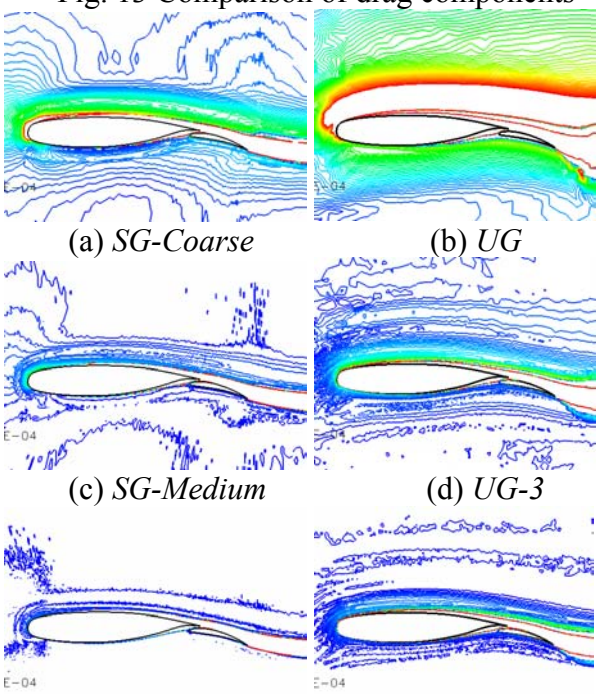

(a) *SG-Coarse* (b) *UG*

(c) *SG-Medium* (d) *UG-3*

(e) *SG-Fine* (f) *UG-8*

Fig. 14 Contours of entropy variation (Range of the contours is extremely narrowed.)

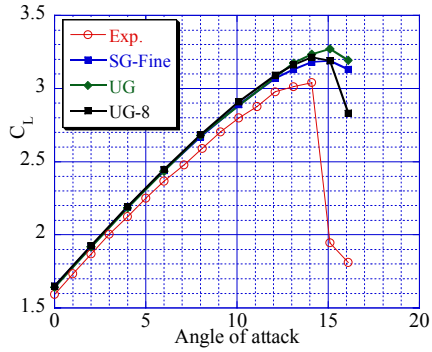

Fig. 15 Variation of C_L-α by mesh density on unstructured mesh

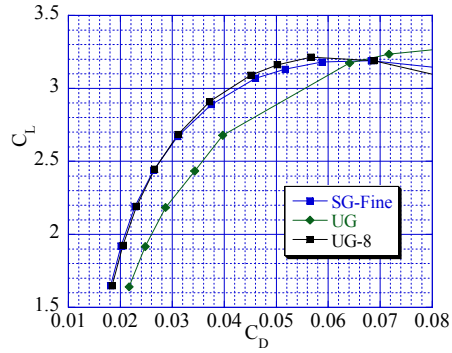

Fig. 16 Variation of C_L-C_D by mesh density on unstructured mesh

3.2 Three-Dimensional Three-Element Wing-Fuselage Configuration

Next, computations of a three-dimensional three-element wing-fuselage configuration are performed.

3.2.1 Computational Model

The geometry used in this study is a trapezoidal high-lift wing [21] shown in Fig. 17. The experiments using this model were performed to produce experimental data for validation and development of CFD methods for three-dimensional high-lift flows [21]. Several computations have been conducted [22] and wind-tunnel interferences have been also investigated [23]. In this wind tunnel test, the model is relatively large and the wind tunnel wall boundaries are closely located. Moreover, this configuration deploying the slat and flap generates much high lift. Therefore, wall-interference corrections were so large.

The configuration of the model used in this study has a slat and a full-span single-slotted flap that extend from wing root to wing tip. The

slat and flap deflections are 30 and 25 degrees, respectively. The mean aerodynamic chord of the model, c, is 39.6 inches and the model semi-span is 85.1 inches. The slat gap and slat height are 0.015c. The flap gap and flap overlap are 0.015c and 0.005c, respectively.

A structured and an unstructured mesh are generated as shown in Fig. 17. The meshes are carefully generated by the information acquired in two-dimensional case. The multi-block structured mesh was generated with the commercial software, Gridgen. The total number of mesh points is about 7.5 million. The number of blocks is 586 blocks. The unstructured mesh was generated with TAS-Mesh. The mesh has about 0.33 million mesh points on the body surface and about 13 million mesh points in volume mesh. The minimum spacing in the normal direction to the wing surface is decided by $0.01/\sqrt{\mathrm{Re}}$ on unstructured mesh and $0.02/\sqrt{\mathrm{Re}}$ on structured mesh. The outer boundary is a semi-sphere whose radius is about 60c.

The unstructured surface meshing using isotropic triangles is semi-automatic and it took only a few hours. However, it requires many mesh points at leading and trailing edge sections. Especially, the trailing edges of this model are bluff and the thickness is very thin. To insert enough number of mesh points using isotropic triangles, a huge number of mesh points are required. Therefore, the trailing edges have only one or two elements on the unstructured mesh as shown in Fig. 17.

3.2.2 Computational Results

In the current computations, freestream Mach number is 0.15 and the Reynolds number is 15×10^6. All turbulent flows are assumed in the computations.

Figures 18 and 19 show C_L-α and C_L-C_D for computed results and experimental data. As for C_L-α, although the both computational results predict C_L slightly higher, the results show good agreement with the experimental data at the moderate angles of attack. As for C_L-C_D, the overall level and the tendency of both computational results agree well with wind-tunnel results. However, some differences of C_D can be seen between computational results and wind tunnel results.

In Fig. 20, C_D is separated into some components, such as C_{Dp}, C_{Df}, C_{Dmain}, C_{Dflap}, C_{Dslat} to investigate the differences. From Fig. 20, the differences are mainly derived from the difference of C_{Dp}. Figures 21 and 22 show a comparison of C_P at α=11.02° and 20.02°. Both computational results are in good agreement with wind tunnel results except for slat components. On the slat, the computational results do not agreement with wind tunnel results, especially near the leading edge of the slat. However, computational results agree with each other. It may be derived from the difference of the stagnation points on the slat because the incidence of the flow is inclined by the wind tunnel wall interferences.

In Figs. 21 and 22, differences of C_P among computations can also be seen near the trailing edge and the wing tip. C_P on unstructured mesh is largely jumped at all trailing edge. It is conceivable that the jumping is derived from the lack of mesh points near the bluff trailing edge. It has possibility to affect the circulation and aerodynamic forces. In addition, near the wing tip, large wing tip vortices are generated as shown in Fig. 23. However, the mesh resolution on the unstructured mesh near the wing tip appears to be lacking.

Figures 24 and 25 show the computed Mach contours at 50% span location. Overall flow structures are almost same. On the unstructured mesh, however, slat wake diffused aft the slat trailing edge and the wake on the flap is spread out. At these moderate angles of attack, the slat effects are not so important and may not affect the aerodynamic forces so much. However, this lack of mesh resolution may lead to inaccurate stall prediction.

In generating the unstructured surface and volume mesh, the mesh resolution near the wing tip and slat wake was much enhanced. The computed aerodynamic forces show fair agreement with experimental results. However, it was shown that further mesh refinement approaches that insert the highly dense mesh in the slat wake and use adaptive mesh refinement are required more accurate prediction.

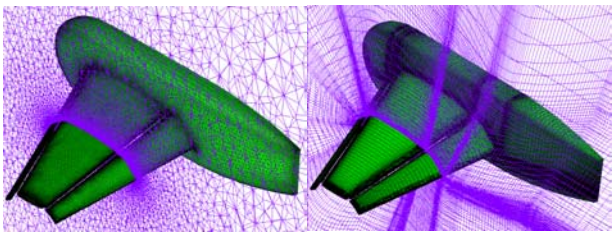

(a) Distant view

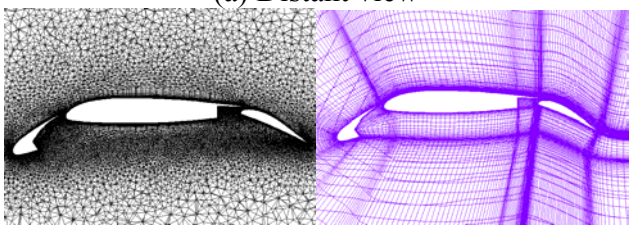

(b) Cut view at 70% span

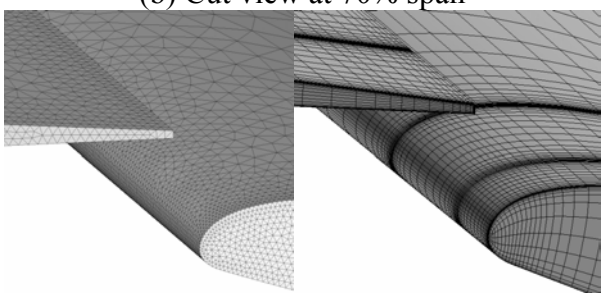

(c) Close-up view near leading edge of flap

Fig. 17 Computational mesh of trapezoidal wing (left: unstructured mesh, right: structured mesh)

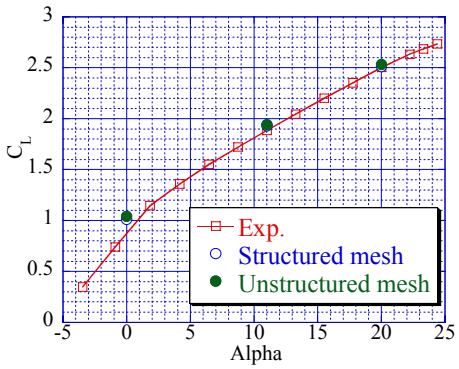

Fig. 18 Comparison of C_L-α between wind tunnel results and computational results

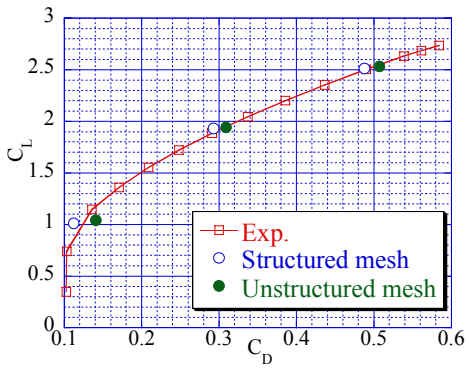

Fig. 19 Comparison of C_L-C_D between wind tunnel results and computational results

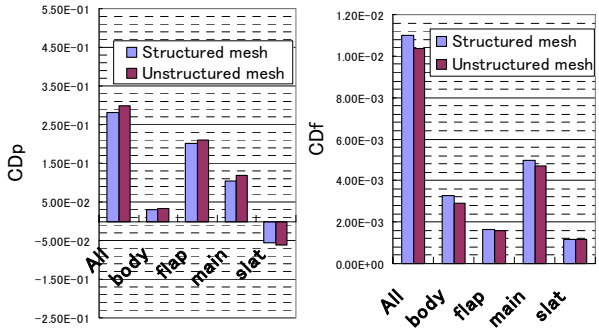

Fig. 20 Comparison of drag components between computational results on structured and unstructured mesh at α=11.02°

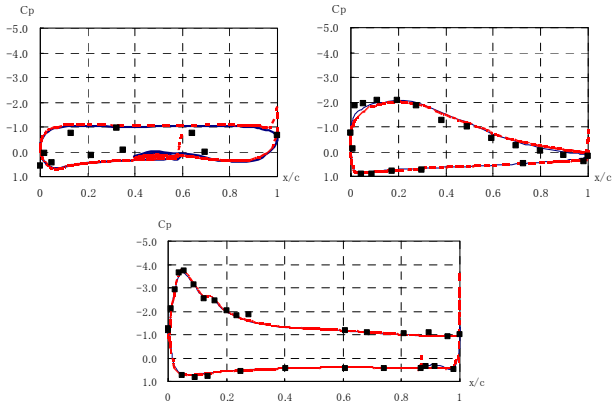

(a) 50% span

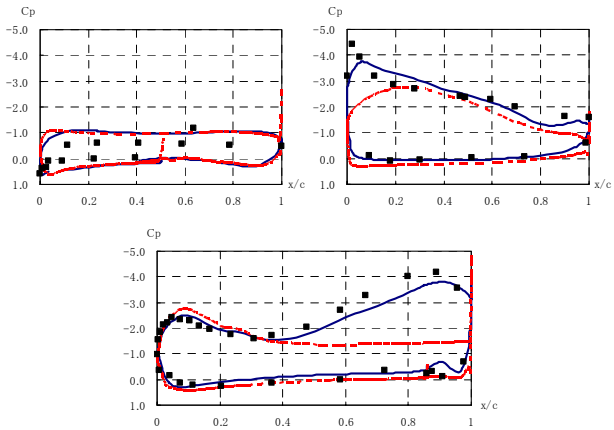

(b) 98% span

Fig. 21 Comparison of C_P at α=11.02°: squares = experiment, blue solid line = structured mesh, red dashed line = unstructured mesh, left = slat, center = main wing, right = flap

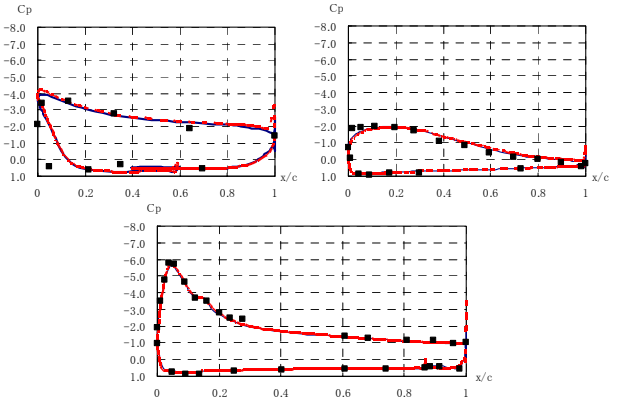

(a) 50% span

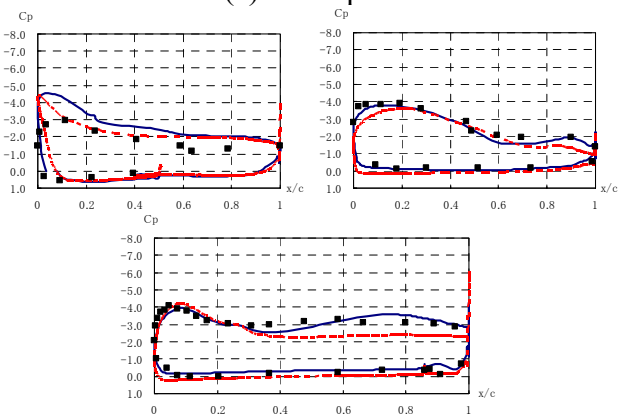

(b) 98% span

Fig. 22 Comparison of C_P at α=11.02°: squares = experiment, blue solid line = structured mesh, red dashed line = unstructured mesh, left = slat, center = main wing, right = flap

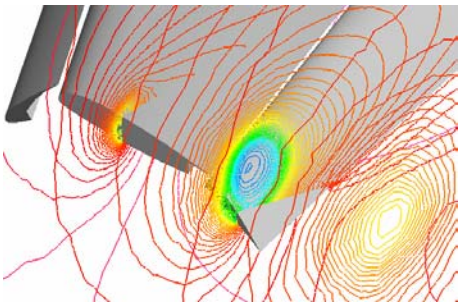

Fig. 23 Pressure contours near wing tip on unstructured mesh

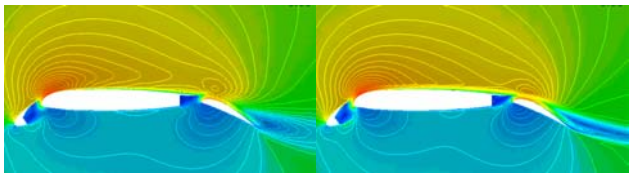

(a) Unstructured mesh (b) Structured mesh
Fig. 24 Mach contours at 50 % span (α=11.02°)

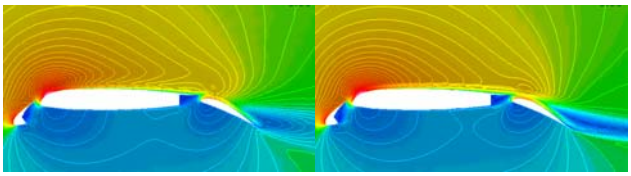

(a) Unstructured mesh (b) Structured mesh
Fig. 25 Mach contours at 50 % span (α=20.02°)

4. Conclusions

For the clarification and improvement of the accuracy of flow analyses around high-lift configurations on structured and unstructured meshes, computations of 2D/3D high-lift configurations have been performed. Computations both on structured and unstructured meshes have been performed and the computational results have been validated.

First, computations of a two-dimensional two-element NLR-7301 airfoil were performed. Influence of locations of outer boundary on the computational results was investigated. It was apparently shown that outer boundaries should be located at least 50-chord length away from the body surface to predict drag. Then, mesh dependency on unstructured meshes was examined by a mesh refinement approach to investigate the difference of computed drag coefficients on a structured mesh and an unstructured mesh. It was shown that the flow analyses on unstructured meshes are comparable to the results on structured meshes by proper distributions of mesh points. The mesh density away from the wing surface was also required for drag prediction by the flows around high-lift devises that have large circulation and wake. Non-physical production of entropy occurred in the regions away from the wing surface where the mesh size was too large to capture the flow changes.

Next, computations of a three-dimensional three-element wing-fuselage configuration were performed. Both computed C_L on structured and unstructured meshes showed good agreement with the experimental data. As for C_D, the overall level agreed well with wind-tunnel results. However, it was also shown that further mesh refinement on unstructured meshes should be used to improve the resolution for slat wake,

wing tip, and trailing edge for more accurate prediction.

References

[1] Meredith, P. T., "Viscous Phenomena Affecting High-Lift Systems and Suggestions for Future CFD Development," *High-Lift Systems Aerodynamics*, AGARD CP 315, Sep. 1993, pp. 19-1 – 19-8.

[2] Kim, S., Alonso, J., and Jameson, A., "Design Optimization of High-Lift Configurations Using a Viscous Continuous Adjoint Method," AIAA Paper 2002-0844, 2002.

[3] Kim, H.-J., Obayashi, S., and Nakahashi, K., "Flap-Deflection Optimization for Transonic Cruise Performance Improvement of Supersonic Transport Wing," *Journal of Aircraft*, Vol. 38, No. 4, July-August 2001, pp. 709-717.

[4] Jeong, S., Murayama, M., and Yamamoto, K., "Efficient Optimization Design Method Using Kriging Model," AIAA Paper 2004-0118, 2004.

[5] Murayama, M., Nakahashi, K., and Matsushima, K., "A Robust Method for Unstructured Volume/Surface Mesh Movement," *Transaction of the Japan Society for Aeronautical and Space Sciences*, Vol. 46, No. 152, Aug. 2003, pp. 104-112.

[6] Murayama, M., Ito, Y., Nakahashi, K., Matsushima, K., and Iwamiya, T. "Viscous Flow Computations of Aircraft with Changing Control Surface Deflection Using Unstructured Grids," AIAA Paper 2003-3660, 2003.

[7] Murayama, M., Nakahashi, K., and Sawada, K., "Simulation of Vortex Breakdown Using Adaptive Grid Refinement with Vortex-Center Identification," *AIAA Journal*, Vol. 39, No. 7, 2001, pp. 1305-1312.

[8] Nakahashi, K., Togashi, F., Fujita, T., and Ito, Y., "Numerical Simulations on Separation of Scaled Supersonic Experimental Airplane from Rocket Booster at Supersonic Speed," AIAA Paper 2002-2843, 2002.

[9] Ito, Y. and Nakahashi, K. "Direct Surface Triangulation Using Stereolithography Data," *AIAA Journal,* Vol. 40, No. 3, pp. 490-496, 2002.

[10] Ito, Y. and Nakahashi, K., "Surface Triangulation for Polygonal Models Based on CAD Data," *International Journal for Numerical Methods in Fluids*, Vol. 39, Issue 1, pp. 75-96, 2002.

[11] Sharov, D. and Nakahashi, K., "A Boundary Recovery Algorithm for Delaunay Tetrahedral Meshing," Proceedings of 5th International Conference on Numerical Grid Generation in Computational Field Simulations, 1996, pp. 229-238.

[12] Ito, Y. and Nakahashi, K., "Unstructured Mesh Generation for Viscous Flow Computations," Proceedings of the 11th International Meshing Roundtable, Ithaca, NY, Sept. 2002, pp. 367-376.

[13] Obayashi, S. and Guruswamy, G. P., "Convergence Acceleration of an Aeroelastic Navier-Stokes Solver," *AIAA Journal*, Vol. 33, No. 6, pp. 1134-1141, 1995.

[14] Sharov, D. and Nakahashi, K., "Reordering of Hybrid Unstructured Grids for Lower-Upper Symmetric Gauss-Seidel Computations," *AIAA Journal*, Vol. 36, No. 3, pp. 484-486, 1998.

[15] Spalart, P. R. and Allmaras, S. R., "A One-Equation Turbulence Model for Aerodynamic Flows," AIAA Paper 92-0439, 1992.

[16] Yamane, T., Yamamoto, K., Enomoto, S., Yamazaki, H., Takaki, R., and Iwamiya, T., "Development of a common CFD platform -UPACS-," Proc. of the Parallel CFD 2000 Conference, Trondheim, Norway, Elsevier Science B. V., 2001, pp. 257-264.

[17] Matsuo, Y., Nakamura, T., Tsuchiya, M., Ishizuka, T., Fujita, N., Ohkawa, H., Hirabayashi, Y., Takaki, R., Yoshida, M., Nakamura, K., Yamamoto, K., Suematsu, K., and Iwamiya, T., "Numerical Simulator III – Building a Terascale Distributed Parallel Computing Environment for Aerospace Science and Engineering," Proc. of the Parallel CFD 2002 Conference, Nara, Japan, Elsevier Science B. V., 2003, pp. 187-194.

[18] Haase, W., et al, "ECARP – European Computational Aerodynamics Research Project: Validation of CFD Codes and Assessment of Turbulence Models," *Notes on Numerical Fluid Mechanics*, Vol. 58, 1997.

[19] Roache, P. J., "Perspective: A Method for Uniform Reporting of Grid Refinement Studies," Journal of Fluids Engineering, Vol. 116, pp. 405-413, 1994.

[20] Sharov, D., and Fujii, K., "Three-Dimensional Adaptive Bisection of Unstructured Grids for Transient Compressible Flow Computations," AIAA Paper 95-1708, 1995.

[21] Johnson, P., Jones, K. M., and Madson, M., " Experimental Investigation of a Simplified 3D High Lift Configuration in Support of CFD Validation," AIAA Paper 2000-4217, 2000.

[22] Nash, S. M. And Rogers, S. E., "Numerical Study of a Trapezoidal Wing High-Lift Configuration," SAE Paper 1999-01-5559, 1999.

[23] Rogers, S. E., Roth, K., and Nash, S. M., "CFD Validation of High-Lift Flows with Significant Wind-Tunnel Effects," AIAA Paper 2000-4218, 2000.